

Article

Development of a DC-Side Direct Current Controlled Active Ripple Filter for Eliminating the Double-Line-Frequency Current Ripple in a Single-Phase DC/AC Conversion System [†]

Ying-Chieh Chen ¹, Liang-Rui Chen ¹, Ching-Ming Lai ^{2,*} , Yuan-Chih Lin ³ and Ting-Jung Kuo ²

¹ Department of Electrical Engineering, National Changhua University of Education, Changhua 500, Taiwan; ycc@ncut.edu.tw (Y.-C.C.); lrchen@cc.ncue.edu.tw (L.-R.C.)

² Department of Electrical Engineering, National Chung Hsing University, Taichung 402, Taiwan; tingjungk@gmail.com

³ Department of Electrical Engineering, National Taiwan University, Taipei 106, Taiwan; gero.lin1980@gmail.com

* Correspondence: pecmlai@nchu.edu.tw

[†] This paper is an extended version of our paper published in IEEE International Conference on Awareness Science and Technology, Taichung, Taiwan, 8–10 November 2017; pp. 234–237.

Received: 30 July 2020; Accepted: 7 September 2020; Published: 12 September 2020



Abstract: The objective of this paper is to propose an active ripple filter (ARF) using the patented DC-side direct current control for eliminating the double-line-frequency current ripple in a single-phase DC/AC conversion system. The proposed ARF and its control strategies can not only prolong the usage life of the DC energy source but also improve the DC/AC system performance. At first, the phenomena of double-line-frequency current ripple and the operation principle of the ARF are illustrated. Then, steady-state analysis, small-signal model, and control loop design of the ARF architecture are derived. The proposed control system includes: (1) a DC current control loop to provide the excellent ripple eliminating performance on the output of the DC energy source; (2) a voltage control loop for the high-side DC-bus voltage of the ARF to achieve good steady-state and transient-state responses; (3) a voltage feedforward loop for the low-side voltage of the ARF to cancel the voltage fluctuation caused by the instability of the DC energy source. Finally, the feasibility of the proposed concept can be verified by the system simulation, and the experimental results show that the nearly zero double-line-frequency current ripple on the DC-side in a single-phase DC/AC conversion system can be achieved.

Keywords: double-line-frequency current ripple; active ripple filter (ARF); single-phase DC/AC

1. Introduction

In recent years, the green energy conversion technologies for distributed generation system have become major industrial developments in the global trend of energy conservation and carbon reduction. Single-phase DC–AC power converters are generally used to supply AC loads in such applications [1–5]. The power generated by DC/AC conversion technologies according to user demands, and is then provided for stand-alone AC loads [6–8] or fed into the utility grid [9].

In a single-phase DC/AC conversion system, the DC input or AC output of the power converter would generate double-line-frequency instantaneous power in addition to the average power. Assuming that all the components of the converter are ideal, according to the law of conservation of energy, the instantaneous power at the DC input must be equal to that at the AC output.

The instantaneous power will cause the energy storage component such as the inductor or capacitor to have double-line-frequency ripples, thus affecting the stability of the DC or AC sides of the power converter [10–25]. As for a further comment in [10], the double-line-frequency current ripple will reduce the lifetime and performance of DC energy source [10], and increase the input filter size. Therefore, the problem of double-line-frequency instantaneous power should not be neglected while developing high performance power converters [11–25].

Previous studies have attempted to use passive or active ripple filters (ARF) to eliminate double-line-frequency instantaneous power. The passive ripple filter increases the size of the energy storage components on the low-voltage or high-voltage sides of the single-phase DC/AC conversion system [9,16], or designs an appropriate inductor–capacitor (LC) series resonant circuit to suppress the double-line-frequency ripple on the high-voltage bus [17]. Although the aforementioned practices can be employed to yield low-current ripple, which are relatively ideal, their main disadvantage is that a considerably large electrolytic capacitor (E-cap) or inductor is required. In addition, the E-cap which is generally paralleled to the low- or high-voltage bus, may heat up due to long-term absorption of ripple components. Moreover, the equivalent series resistor (ESR) heats up along with the larger ripples on the E-cap, which not only causes the additional power consumption, but also reduces the lifetime of E-cap [20,21].

ARF technique is the power electronics circuit with energy storage elements [4] for eliminating the problem of double-line-frequency instantaneous power, and the power decoupling method is commonly used for the control strategy of the ARF [4,5]. Therefore, considering the size, cost, and characteristics of passive components, passive ripple filters have been gradually replaced by the ARF [11–15,18–25]. As a reference for research origin, the general ARF scheme and its conventional control diagrams for the single-phase DC/AC conversion system applications are shown in Figure 1.

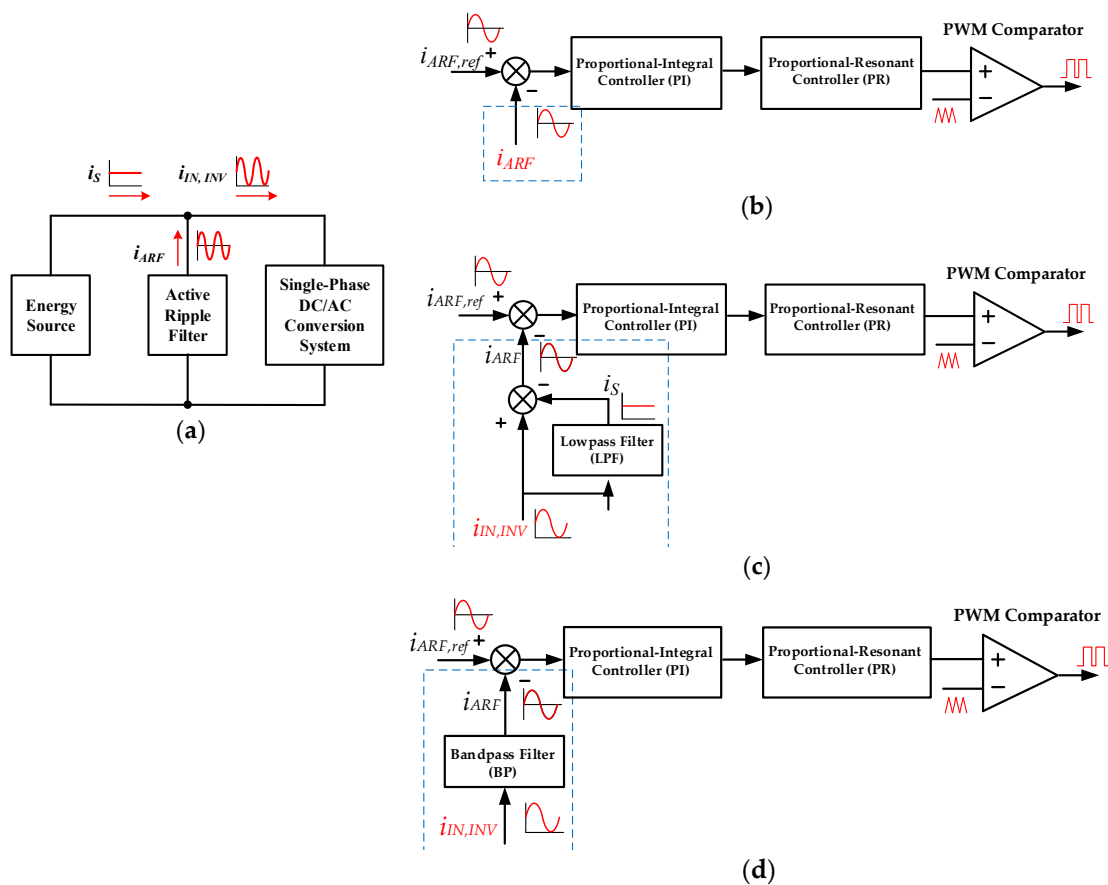


Figure 1. The general ARF scheme (a); and its conventional control diagrams (b–d) for the single-phase DC/AC conversion system applications.

According to the different current measurement locations of the ARF as shown in Figure 1a, the conventional control diagram of the ARF can be classified into (1) the input current sensing point of the ARF, as shown in Figure 1b; and (2) the input current sensing point of the single-phase DC/AC power conversion system, as shown in Figure 1c,d. For locating the input current sensing point of the ARF, the proportional-resonant (PR) controller and the proportional-integral (PI) controller are cascade interconnection to achieve the zero steady-state error for tracking AC reference. For locating the input current sensing point of the single-phase DC/AC power conversion system, it requires the low pass filter (Figure 1c) or bandpass filter (Figure 1d) to filter the DC component of the input current of the single-phase DC/AC power conversion system. In summary, the ARF must provide AC current, which is difficult to control, and the above-mentioned methods cause the design process of system controller as well as its parameters more complicated and difficult indeed.

In this study, an ARF using the DC-side direct current control for eliminating the double-line-frequency current ripple in a single-phase DC/AC conversion system would be proposed. Compared with the other conventional control diagrams as shown in Figure 1b–d, the DC-side direct current control strategy is relatively simple to implement. The current command and feedback signals are DC values, hence the nearly zero-steady state error can be fulfilled easily. The steady-state analysis, small-signal model and control loop design of the proposed ARF architecture are derived.

2. Principle of Double-Line-Frequency Instantaneous Power

Figure 2 illustrates a single-phase DC/AC conversion system, and characteristic waveforms of the system for the power flows without and with the ARF are presented in Figure 3.

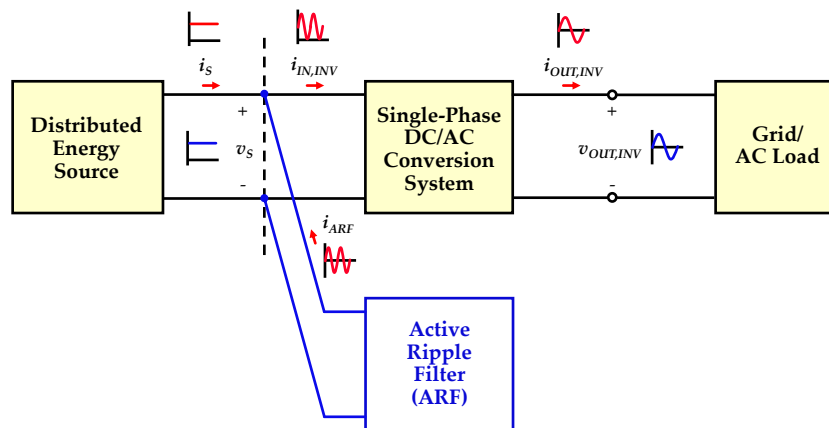


Figure 2. Integration of the ARF into a single-phase DC/AC conversion system [26].

The key waveforms without the ARF are shown in Figure 3a. In this figure, the instantaneous output voltage, output current, and output power of the single-phase DC/AC conversion system are expressed as $v_{OUT,INV}$, $i_{OUT,INV}$, and $p_{OUT,INV}$, respectively, as follows:

$$v_{OUT,INV} = V_m \sin(\omega_L t) \quad (1)$$

$$i_{OUT,INV} = I_m \sin(\omega_L t) \quad (2)$$

$$P_{OUT,INV} = v_{OUT,INV} \cdot i_{OUT,INV}. \quad (3)$$

According to the conservation of energy and the assumption that the energy dissipation of the system can be neglected, the output power of the energy source p_S can be expressed as follows:

$$p_S = p_{OUT,INV} = P_S + p_R \quad (4)$$

$$P_S = \frac{V_m I_m}{2} \quad (5)$$

$$p_R = \frac{V_m I_m}{2} \cos(2\omega_L t \pm \pi) \quad (6)$$

where P_S is the average power and p_R refers to the double-line-frequency ripple power generated by the product of $v_{OUT,INV}$ and $i_{OUT,INV}$.

Assuming that the energy source provides pure DC voltage (i.e., $v_S \approx V_S$), and the output current of the energy source can be derived as follows:

$$i_S = I_S + i_R = \frac{P_S}{V_S} + \frac{P_S}{V_S} \cos(2\omega_L t \pm \pi) \quad (7)$$

where I_S and i_R refer to the DC current and the AC (ripple) current provided by the energy source, respectively.

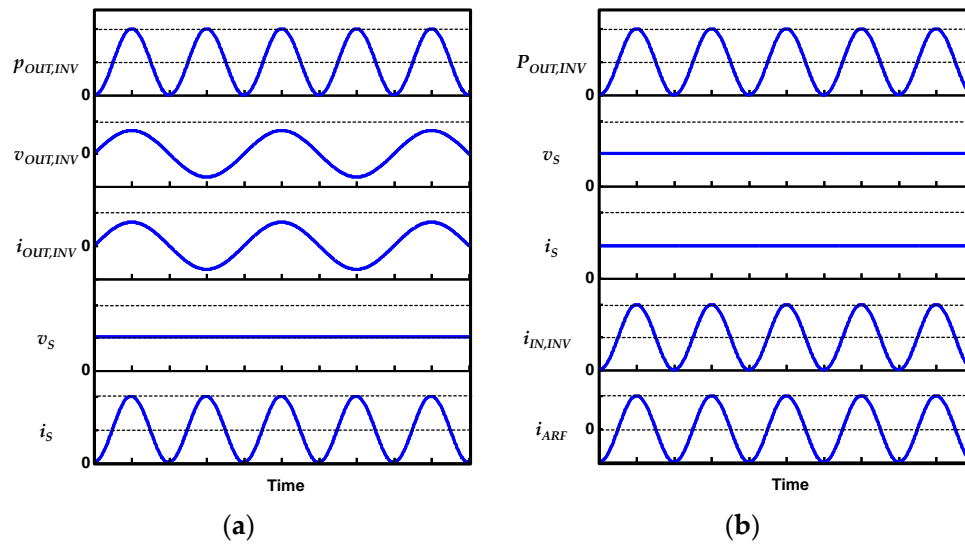


Figure 3. Key waveforms to illustrate the operating principles for double-line-frequency components of a single-phase DC/AC conversion system [26]: (a) without the ARF and (b) with the ARF.

According to (7), the double-line-frequency ripple power generated by the single-phase DC/AC conversion system was completely reflected on the current provided by the energy source. As a result, the current ripple would suffer the performance of the energy source and substantially reduce its service life [27–30]. Figure 3b illustrates the key waveforms of the single-phase DC/AC conversion system after the integration of the ARF. In this figure, $i_{IN,INV}$ and i_{ARF} are respectively defined as the input current of the single-phase DC/AC conversion system and the compensating current provided by the ARF. It can be seen from Figure 2, $i_{IN,INV}$ can be directly expressed as follows:

$$i_{IN,INV} = I_S + i_{ARF}. \quad (8)$$

The double-line-frequency ripple components of were provided by the ARF, as shown in (9):

$$i_{ARF} = i_R = \frac{P_S}{V_S} \cos(2\omega_L t \pm \pi). \quad (9)$$

3. Operating Principles of the ARF

The ARF must possess the ability of bidirectional power flow to provide double-line-frequency current ripple and thus yield a pure DC current of the energy source. As shown in Figure 4, the circuit architecture of the ARF is a bidirectional buck-boost converter. The polarities of the output current of

the ARF can be divided into the boost and buck modes. When the polarity of the output current is positive, the ARF operates in a buck mode. By contrast, when the polarity of the output current is negative, the ARF operates in a boost mode.

The assumptions are made in analyzing the ARF:

- (1) the ARF operates in continuous conduction mode (CCM);
- (2) the drive signals for active switches Q_1 and Q_2 of the ARF are respectively defined as d_1 and d_2 ;
- (3) the DC-bus voltage $v_{DC,ARF}$ could be approximated as a constant value, i.e., $v_{DC,ARF} \approx V_{DC,ARF}$;
- (4) all voltages and currents in the ARF are periodic in steady-state condition; for simplicity, it is assumed that all the components of the ARF in Figure 4 are idealized.

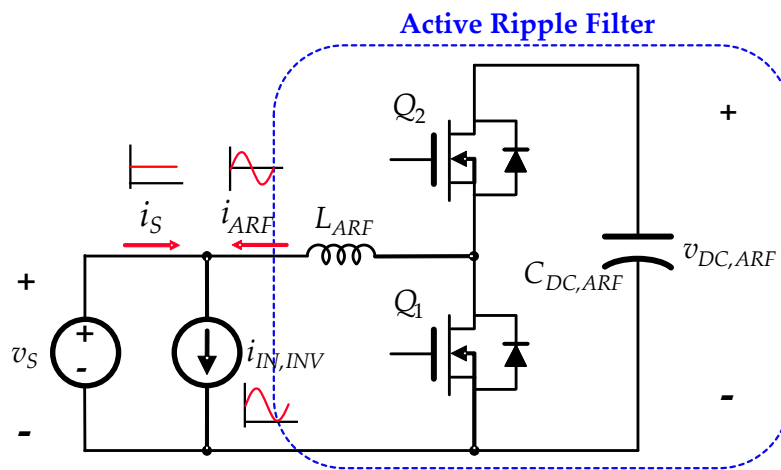


Figure 4. Circuit architecture of the ARF.

3.1. Buck Mode

Figure 5a illustrates the circuit architecture of the ARF operated in the buck mode. When Q_1 was turned off and Q_2 was turned on, the relation between current i_{ARF} and voltage of inductor L_{ARF} can be calculated using the equation as follows:

$$\frac{di_{ARF}}{dt} = \frac{V_{DC,ARF} - V_S}{L_{ARF}} \quad (10)$$

when Q_1 was turned on and Q_2 was turned off, the relation between current i_{ARF} and voltage of inductor L_{ARF} can be calculated using the equation as follows:

$$\frac{di_{ARF}}{dt} = -\frac{V_S}{L_{ARF}}. \quad (11)$$

According to the volt-second balance principle of the inductor L_{ARF} , the voltage conversion ratio between the low-voltage and high-voltage sides of the ARF can be derived as follows:

$$\frac{V_{DC,ARF}}{V_S} = \frac{d_1 + d_2}{d_2}. \quad (12)$$

3.2. Boost Mode

Figure 5b illustrates the circuit architecture of the ARF operated in the boost mode. When Q_1 was turned off and Q_2 was turned on, the relation between current i_{ARF} and voltage of inductor L_{ARF} can be calculated using the equation as follows:

$$\frac{di_{ARF}}{dt} = -\frac{V_S - V_{DC,ARF}}{L_{ARF}} \quad (13)$$

when Q_1 was turned on and Q_2 was turned off, the relation between current i_{ARF} and voltage of inductor L_{ARF} can be calculated using the equation as follows:

$$\frac{di_{ARF}}{dt} = -\frac{V_S}{L_{ARF}}. \quad (14)$$

Likewise, according to the volt-second balance principle of inductor L_{ARF} , the result of (12) was also applicable to the boost mode due to the ARF has the bidirectional power flow characteristic. If the drive signals of switches Q_1 and Q_2 are assumed to be complementary (i.e., $d_1 = 1 - d_2$), then the voltage conversion ratio of the ARF can be simplified as follows:

$$\frac{V_{DC,ARF}}{V_S} = \frac{1}{1 - d_1}. \quad (15)$$

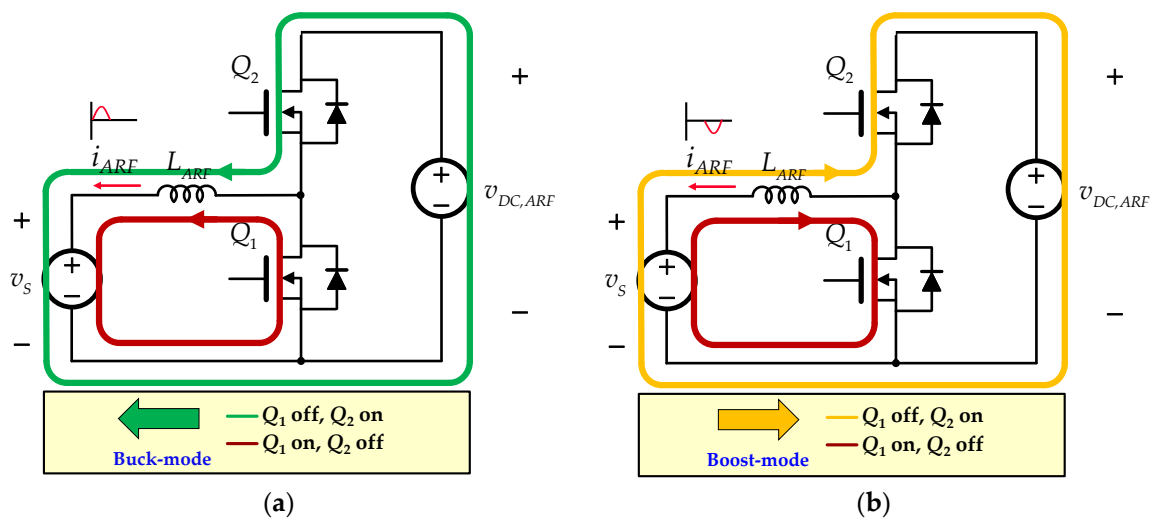


Figure 5. Circuit architecture of the ARF [26]: (a) the buck mode and (b) the boost mode.

4. Control Strategy of the ARF

Figure 6 illustrates the developed control system for the ARF. At first, it can be seen that the DC-bus voltage ($v_{DC,ARF}$) is sensed and compared with the voltage reference to produce an error signal. Second, the voltage controller receives the error signal to produce the average power reference signal, $p_{s,ref}$, which is divided by the feedforward compensation signal (i.e., energy source voltage, v_S) to generate the current reference, $i_{S,ref}$. In the inner current control loop, the energy source current (i_S) is sensed and compared with the current reference to generate the modulated signal (v_{con}) of the pulse width modulation (PWM) generator.

It is noted that the ARF must provide AC current (i.e. ripple current), which is difficult to control. In this study, the current reference and the sensed signals are all DC value, hence the nearly zero-steady state error can be fulfilled easily. In other words, this study proposes a method of indirectly regulating the output AC current of the ARF by directly controlling the input DC current of the energy source. According to Figure 7, the controller design of the outer voltage loop and inner current loop of the ARF was illustrated as follows.

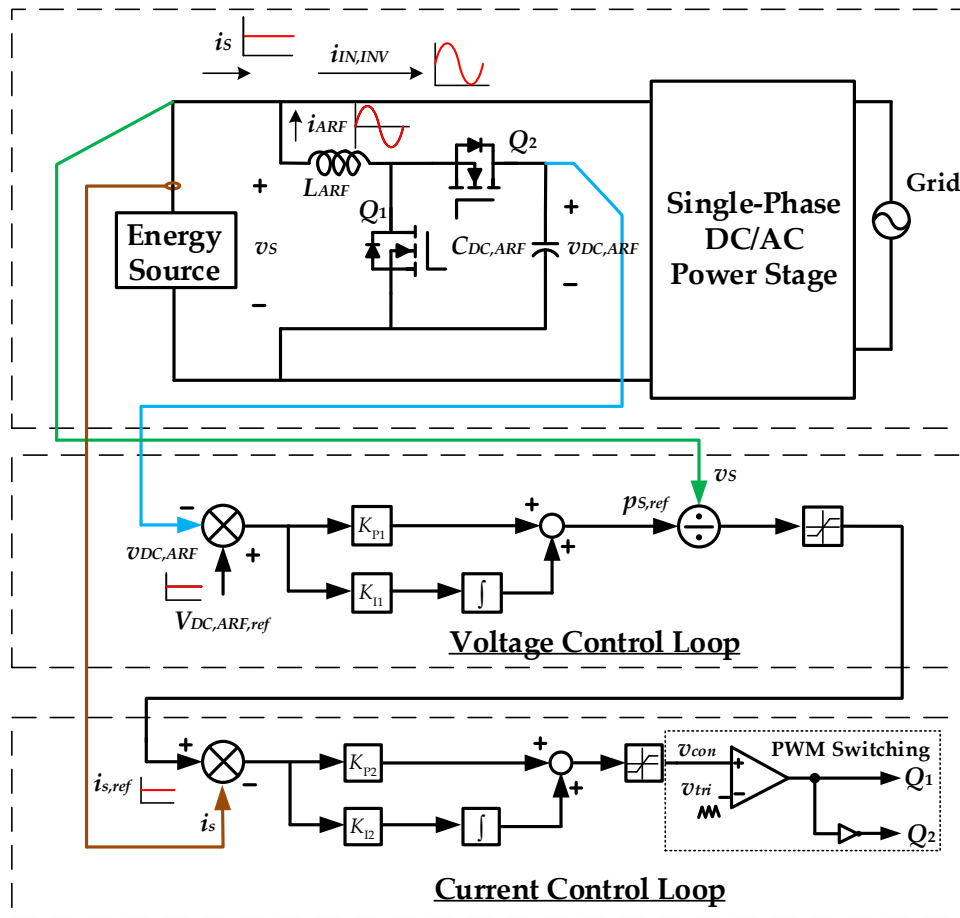


Figure 6. The developed control system for the ARF.

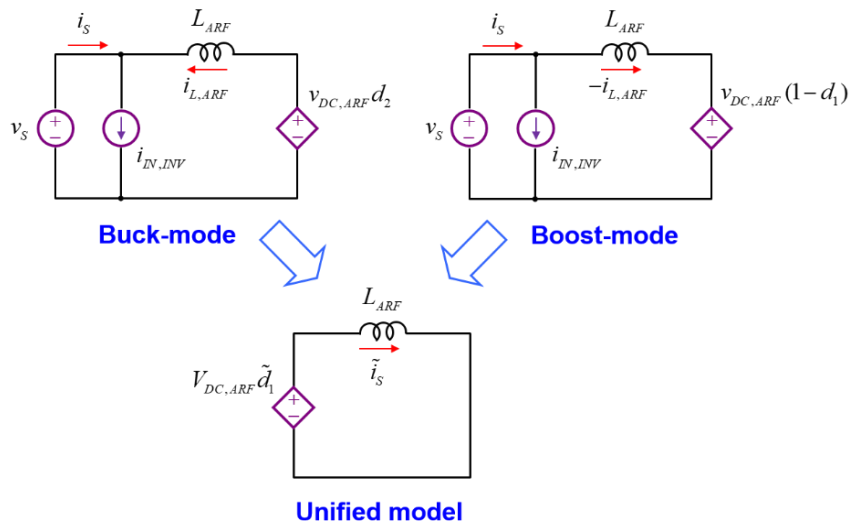


Figure 7. Small-signal equivalent circuit of the current loop.

4.1. Designing the Controller of the Current Loop

Considering the buck mode operation, the inductor voltage in one switching period can be expressed as follows:

$$v_{L,ARF} = L_{ARF} \frac{di_{L,ARF}}{dt} = v_{DC,ARF} d_2 - v_s. \quad (16)$$

Perturbation was introduced into the inductor current and the drive signal d_2 of Q_2 , and $d_1 = 1 - d_2$. This study assumed that v_S and $v_{DC,ARF}$ operated in a stable DC status. Thus, (16) can be rewritten as follows:

$$L_{ARF} \frac{d\tilde{i}_{L,ARF}}{dt} = -V_{DC,ARF} \tilde{d}_1 \quad (17)$$

when the converter was operated in the boost mode, the inductor voltage in one switching cycle can be expressed as:

$$v_{L,ARF} = L_{ARF} \frac{di_{L,ARF}}{dt} = v_{DC,ARF}(1 - d_1) - v_S. \quad (18)$$

Perturbation was introduced into the inductor current and the drive signal d_1 of Q_1 . Similarly, v_S and $v_{DC,ARF}$ were assumed to operate in a stable DC status.

Accordingly, (18) can be further expressed as:

$$L_{ARF} \frac{d(\tilde{i}_{L,ARF})}{dt} = -V_{DC,ARF} \tilde{d}_1. \quad (19)$$

An observation of (17) and (19) indicated that the small-signal models derived in the buck and boost operational modes were the same. In addition, this study controlled the output current of the ARF indirectly by controlling the output current of the energy source to regulate the required current ripple provided by the ARF. Therefore, the derived small-signal model must undergo minor modifications. According to (8), the three branch currents of the input side of the ARF-integrated single-phase DC/AC conversion system were interrelated. This study assumed that the input current $i_{IN,INV}$ required by the single-phase DC/AC conversion system can be regarded as a definite value in consideration of small signals. In other words, perturbation in the current provided by the energy source would be directly reflected on the output current of the ARF.

Therefore, the introduction of perturbation into the two signals in (8) would result in the following equation:

$$\tilde{i}_S = -\tilde{i}_{L,ARF}. \quad (20)$$

Substituting (17) or (19) into the equation, performing the Laplace transform, and deriving the transfer function of the small-signal model of the current loop is as follows:

$$G_c = \frac{\tilde{i}_S}{\tilde{d}_1} = \frac{V_{DC,ARF}}{sL_{ARF}}. \quad (21)$$

The equivalent circuit derived in the aforementioned process is illustrated in Figure 7. The parameters were $V_{DC,ARF} = 100$ V and $L_{ARF} = 250$ μ H, and the open-loop gain of the current loop is expressed as (22).

$$L_c(s) = \frac{\tilde{i}_s}{\tilde{v}_{con}} = F_m G_c(s) = \frac{4000}{s} \quad (22)$$

where F_m is the equivalent small-signal gain of pulse-width modulation, as follows

$$F_m = \frac{1}{V_{tri}} = \frac{1}{100} \quad (23)$$

where V_{tri} is the peak value of the carrier wave of the PWM generator.

According to Figure 7, the open-loop gain of the current loop was in a first-order integral form. Therefore, the controller only needed to be in a proportional-integral (PI) form to achieve satisfactory control. The form and parameters of the designed PI controller are presented as follows:

$$C_c(s) = K_{P1} + \frac{K_{I1}}{s} = K_{pc} \cdot \frac{s + z_c}{s} = 4.5 \cdot \frac{s + 10000}{s}. \quad (24)$$

After incorporating the compensation from the controller, the open-loop gain of the current loop is expressed as follows:

$$T_c(s) = C_c(s)L_c(s) = 18000 \cdot \frac{s + 10000}{s^2}. \quad (25)$$

The bode plot of the response frequency of the current loop after receiving compensation from the controller is also illustrated in Figure 8. According to the figure, the zero crossover frequency (i.e., closed-loop bandwidth) was 3 kHz, and the phase margin was 60°. In other words, the closed-loop control enabled the ARF to attain sufficient response and stability.

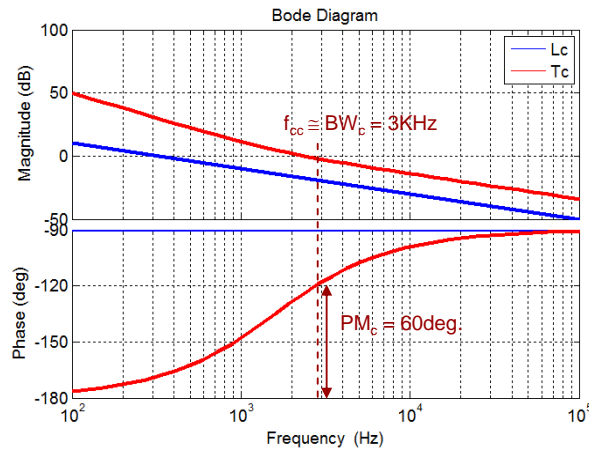


Figure 8. Bode plot of the frequency response of the current loop.

4.2. Designing the Controller of the Voltage Loop

In practice, the capacitor voltage on the high-voltage side of the ARF also involved double-line-frequency components. Consequently, the compensation current command may be affected through feedback control, resulting in the failure to completely eliminate the double-line-frequency components at the output side of the single-phase DC/AC conversion system. To prevent this problem, the bandwidth of the voltage loop on the high-voltage side of the ARF must be substantially lower than the double-line-frequency to ensure that the current command remains unaffected.

According to Figure 9, the small-signal model of the voltage loop was derived as follows from the perspective of power, where p_{CH} and i_{CH} refer to the power and current of the capacitor energy storage on the high-voltage side of the ARF.

$$p_{RIP} = p_{IN,INV} - p_S = -p_{CH} \quad (26)$$

$$v_S i_{L,ARF} = -v_{DC,ARF} i_{CH}. \quad (27)$$

Assuming the stable operation of v_S and $v_{DC,ARF}$, to consider (20) and substitute perturbation into i_S and i_{CH} . Thus, (27) can be rewritten as:

$$\frac{\tilde{i}_{CH}}{\tilde{i}_S} = \frac{V_S}{V_{DC,ARF}}. \quad (28)$$

Multiplying (28) by the capacitive resistance on the high-voltage side, to perform the Laplace transform, and then the transfer function of the small-signal model of the voltage loop can be expressed as follows:

$$G_v = \frac{\tilde{v}_{DC,ARF}}{\tilde{i}_S} = \frac{V_S}{s V_{DC,ARF} C_{DC,ARF}}. \quad (29)$$

The parameters of the small-signal model of the voltage loop included $v_S = 36$ V, $V_{DC,ARF} = 100$ V, and $C_{DC,ARF} = 3400$ μ F. The open-loop gain of the voltage loop is as follows:

$$L_v(s) = \frac{\tilde{v}_{DC,ARF}}{\tilde{p}_{S,ref}} = \frac{P_v(s)}{V_S} = \frac{2.941}{s}. \quad (30)$$

Notice that (30), which includes the feedforward term of the s at denominator, which can eliminate fluctuation caused by v_s . Similar to the current loop, the open-loop gain of the voltage loops was in a first-order integral form as well. Therefore, the PI form can be used on the controller. The parameters of the controller are expressed as follows:

$$C_v(s) = K_{P2} + \frac{K_{I2}}{s} = K_{pv} \cdot \frac{s + z_v}{s} = 16 \cdot \frac{s + 20}{s}. \quad (31)$$

After incorporating the compensation from the controller, the open-loop gain of the voltage loop is presented as follows:

$$T_v(s) = C_v(s)L_v(s) = 47.05 \cdot \frac{s + 20}{s^2}. \quad (32)$$

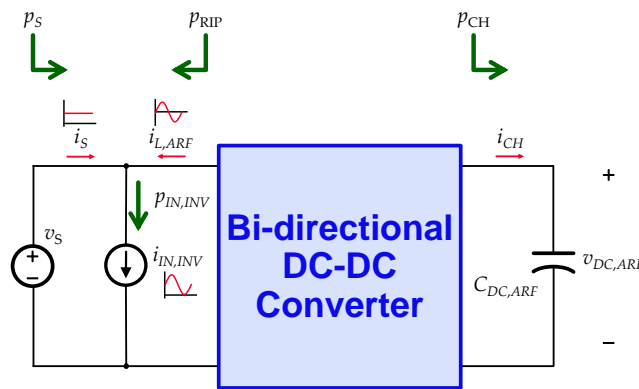


Figure 9. Small-signal equivalent circuit of the voltage loop.

Figure 10 illustrates the open-loop gain of the voltage loop before and after compensation. The figure shows that, after compensation, the zero crossover frequency was 8 Hz and the phase margin was 68°. The closed-loop control improved the stability of the capacitor voltage on the high-voltage side of the ARF.

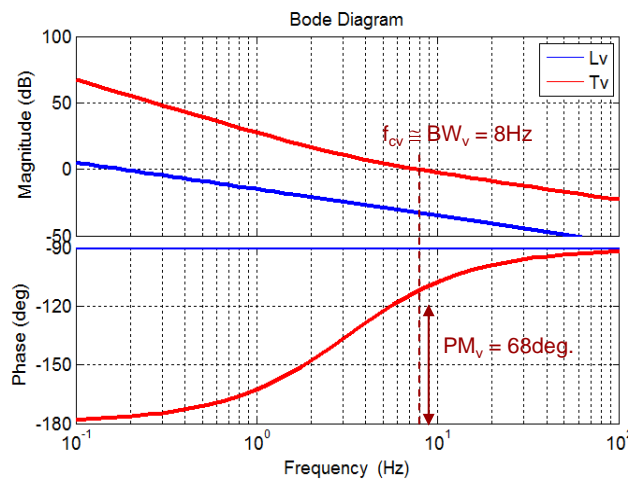


Figure 10. Bode plot of the response frequency of the voltage loop.

5. Simulation and Experimental Results

MATLAB© and PSIM© software were used to analyze and verify the feasibility of the proposed method. The specifications of the system are listed as follows: an input DC voltage of 36 V for the distributed energy source, an output AC voltage of 110 Vrms, and a rated power output of 500 W for single-phase DC/AC grid-connected operation [31]. The experimental platform was implemented,

as shown in Figure 11. The parameters of circuit components and the specification of the experimental platform are listed in Tables 1 and 2, respectively.

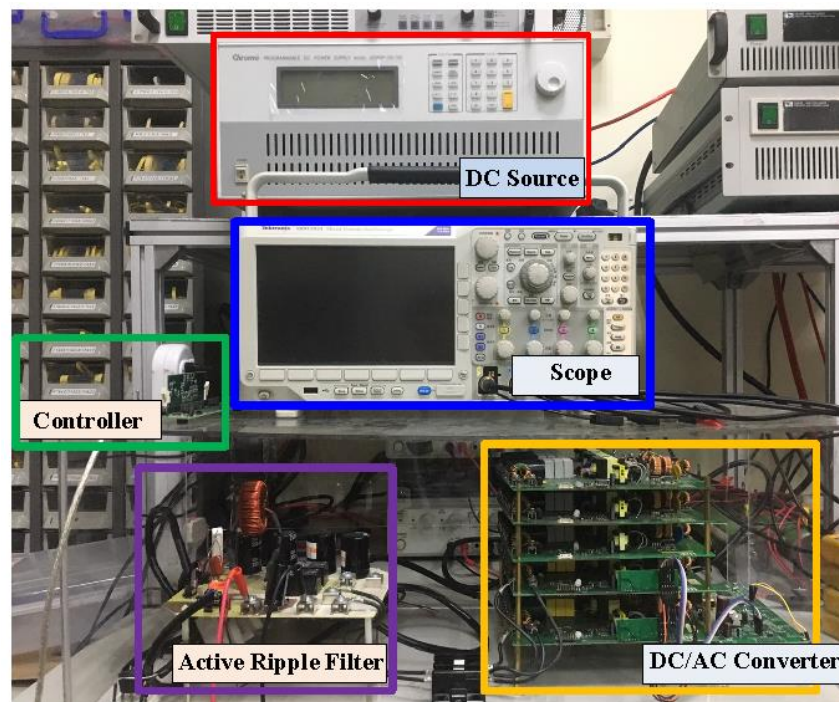


Figure 11. Experimental platform of a 500 W single-phase DC/AC conversion integrated with ARF.

Table 1. Component parameters of the ARF circuit.

Component	Symbol	Value/Model
Inductance	L_{ARF}	250 μ H
MOSFET	Q_1, Q_2	FDA59N30
Capacitance	$C_{DC, ARF}$	3400 μ F/250V

Table 2. Equipment of the experimental platform.

Type	Model
DC Source	Chroma 62050P-100-100
Scope	Tektronix MDO3024
Power Analyzers	Yokogawa WT310

The simulation and experimental results at 500 W before the ARF were integrated into the distributed energy source as shown in Figure 12a,b, respectively. The distributed energy source provides an average current of 13.85 A, the peak-to-peak value of the double-line-frequency current ripple is 24 A.

The only difference is that the peak value of the output current of the single-phase DC/AC conversion system are 6.3 A and 5.8 A, respectively. As shown in the results, the ripples strongly affect the service life of the DC energy source and reduces the operating efficiency of the power system.

Next, after integration of the ARF, the double-line-frequency current ripple is suppressed, the average current is 14 A and 14.25 A, the peak-to-peak value of the inductor current is 23 A and 22 A, the results are shown in Figure 13a,b, respectively. In this case, the life service of the distributed energy source not only increased, but the performance of the power system was also enhanced.

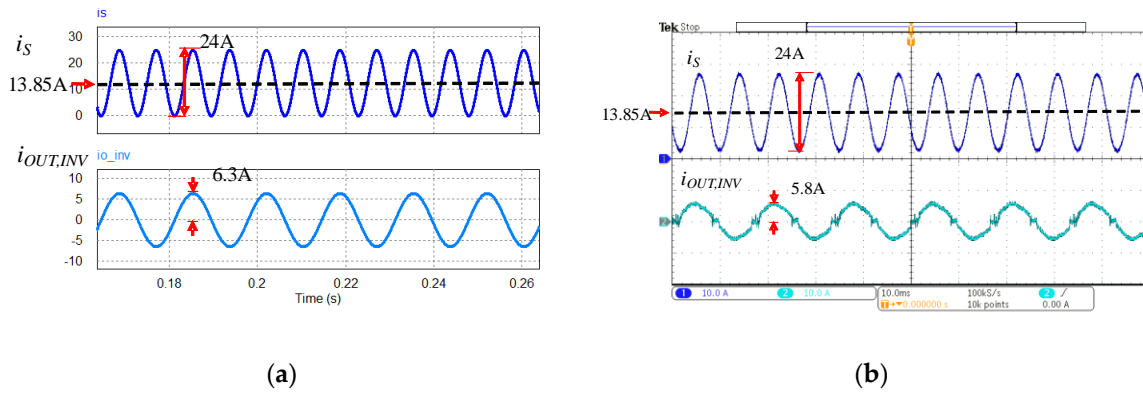


Figure 12. The output currents of the distributed energy source before the ARF was integrated: (a) Simulation result and (b) experimental result.

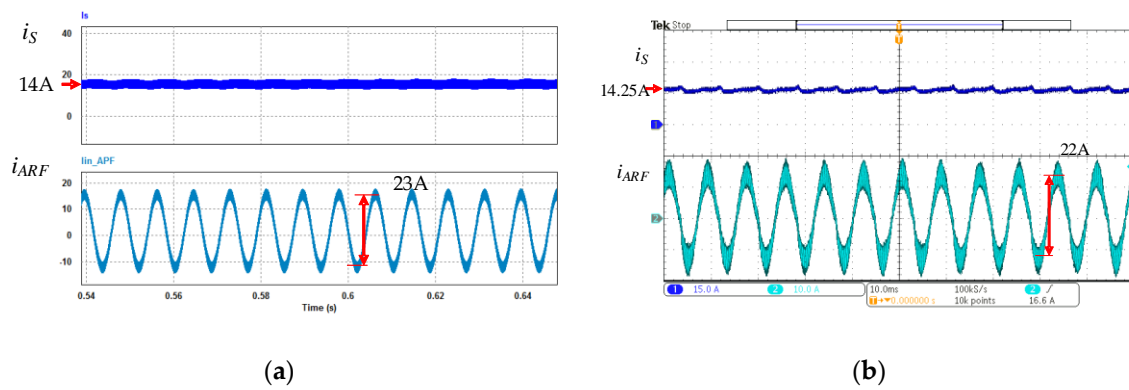


Figure 13. Steady-state of the output voltage and inductor current of the ARF: (a) Simulation result and (b) experimental result.

Figure 14 shows the simulation and experimental results of the DC/AC output voltage and output current at 500 W when the ARF was integrated, respectively. In Figure 14a (simulation), the peak voltage of 155.7 V, the peak value of the output current is 6.25 A. In Figure 14b (experiments), the peak current of the output current is 5.8 A.

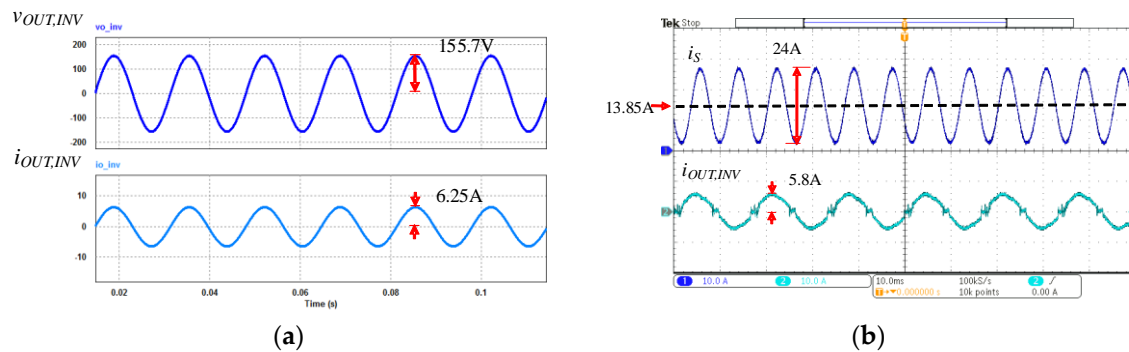


Figure 14. The output voltage and current of the proposed single-phase DC/AC conversion system. (a) Simulation result and (b) experimental result.

To add a soft-start circuit made the output of the system start up smoothly, the current remained stable, the output voltage increased to 100 V smoothly without overshoot, and the soft-start time was about 0.55 s. The results are shown in Figure 15a,b, respectively.

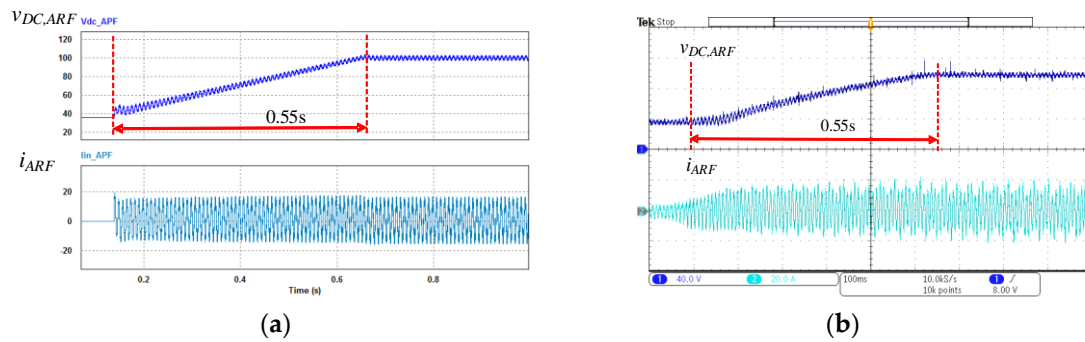


Figure 15. The bus voltage and inductor current of the ARF during the soft start process: (a) Simulation result and (b) experimental result.

As seen in Figures 12–15, the simulation coincided with experimental results to validate the proposed method. These results correspond with the calculations in the steady-state analysis as well. Figure 16a illustrates spectrum of the input current at 120 Hz before the integration of ARF and Figure 16b verifies the double-line-frequency current ripple of the input side is significantly reduced.

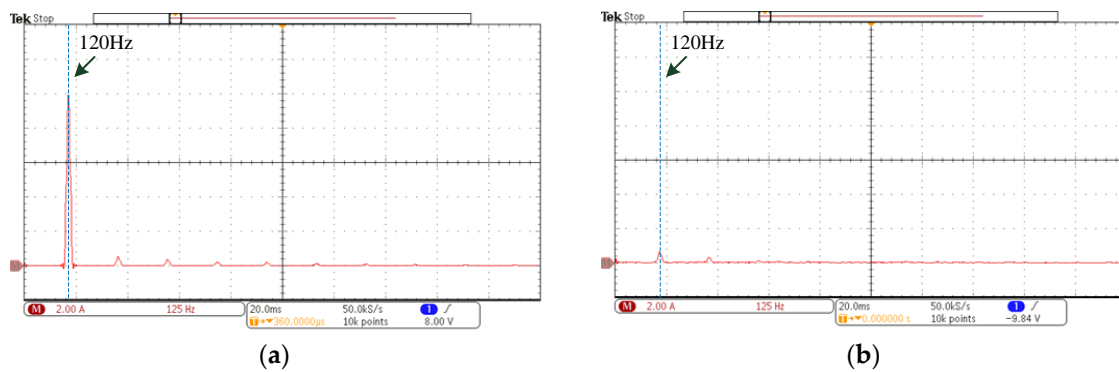


Figure 16. Experimental results of measurement input DC current spectrum in 120Hz: (a) before DC energy source integrates with ARF and (b) DC energy source integrates with ARF.

By observing Figure 17, in the full load case, the peak-to-peak current ripple is 24 A, which is 175% of the average value. When ripple suppression was enabled, the peak-to-peak current ripple reduced to 2 A, which was 14% of the average value. Therefore, it can be proved that energy source was integrated with ARF and the double-line-frequency current ripple of the energy source could be significantly reduced. Figure 18 show that the highest conversion efficiency is about 97%.

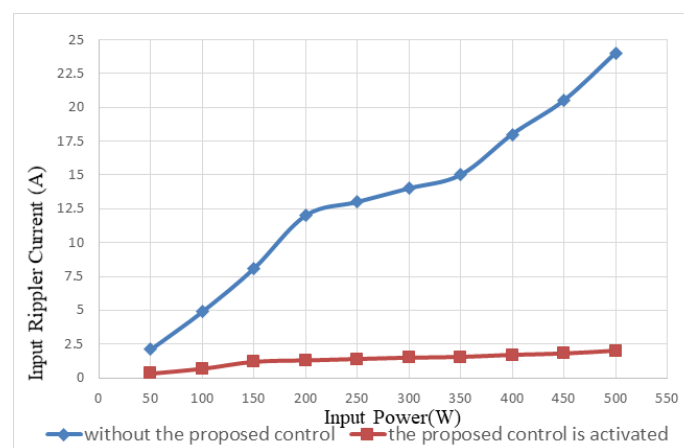


Figure 17. Measured results are compared with proposed method under different loads.

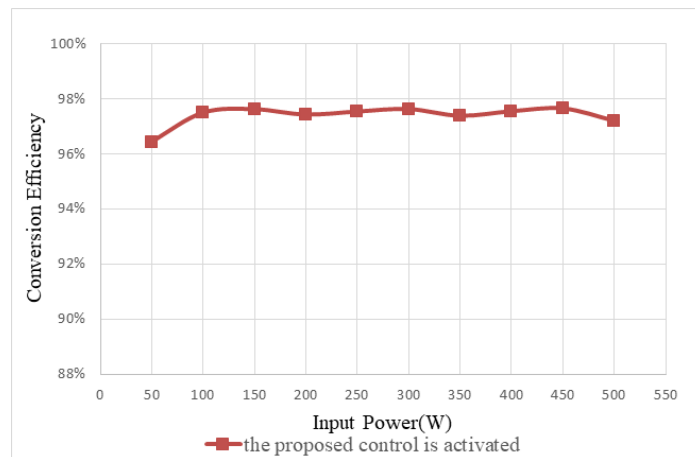


Figure 18. Conversion efficiency of the proposed method under different loads.

Finally, the comparison dataset for the system integrated with, and without the ARF, the actual efficiencies are measured by a WT310 power analyzer under different loads, as listed in Table 3.

Table 3. Measured ARF dataset.

Without Proposed ARF				With Proposed ARF			
V_S (V)	I_S (A)	$I_{S,RIP-pp}$ (A)	P_S (W)	I_S (A)	$I_{S,RIP-pp}$ (A)	P_S (W)	η (%)
36	1.35	2.1	48.6	1.4	0.35	50.4	96.4
36	2.72	4.9	97.92	2.79	0.7	100.44	97.4
36	4.1	8.1	147.6	4.2	1.2	151.2	97.6
36	5.67	12	204.12	5.82	1.3	209.52	97.4
36	7.12	13	256.32	7.3	1.4	262.8	97.5
36	8.22	14	295.92	8.42	1.5	303.12	97.6
36	9.66	15	347.76	9.92	1.55	357.12	97.3
36	11.12	18	400.32	11.4	1.7	410.4	97.5
36	12.45	20.5	448.2	12.75	1.8	459	97.6
36	13.85	24	498.6	14.25	2	513	97.1

6. Conclusions

In this paper, simulations and experiments were carried out to demonstrate that the proposed ARF and its DC-side direct current control system structure could be potentially applied to produce a zero-ripple input current single-phase DC/AC architecture (patented [32,33]). The proposed control system has a DC current control loop, a voltage control loop, and a voltage feedforward control loop. The efficacy of the proposed method is verified experimentally under steady-state conditions. The results show that the proposed ARF and its control strategies offers many advantages, such as a fast dynamic response, simple implementation, a nearly zero-steady state error, and the elimination of the double-line-frequency current ripple in a single-phase DC/AC conversion system above 90%.

Author Contributions: C.-M.L. and Y.-C.C. substantially contributed to the examination and interpretation of the results, development of the overall system, and review and proofreading of the manuscript. L.-R.C. substantially contributed to the review and proofreading of the manuscript. Y.-C.L. and T.-J.K. substantially contributed to literature search, control strategy design, and production and analysis of the results. All authors have read and agreed to the published version of the manuscript.

Funding: This work was supported in part by the Ministry of Science and Technology (MOST), Taiwan, under grant MOST-107-2221-E-005-079-MY3, MOST-108-2218-E-005-021, and MOST 109-3116-F-006-020-CC1.

Acknowledgments: The authors would like to express their appreciation to Quan-Sheng Lin (guided by Ching-Ming Lai) for the experimental platform setup.

Conflicts of Interest: The authors declare no conflict of interest.

References

1. Amin, S.; Lee, H.H.; Choi, W. A novel power decoupling control method to eliminate the double line frequency ripple of two stage single-phase DC-AC power conversion systems. *Electronics* **2020**, *9*, 913. [\[CrossRef\]](#)
2. Zhang, J.; Ding, H.; Wang, B.; Guo, X.; Padmanaban, S. Active power decoupling for current source converters: An overview scenario. *Electronics* **2019**, *8*, 197. [\[CrossRef\]](#)
3. Cai, Y.; Xu, J.; Yang, P.; Liu, G. Design of double-line-frequency ripple controller for quasi-single-stage AC-DC converter with audio susceptibility model. *IEEE Trans. Ind. Electron.* **2019**, *66*, 9226–9237. [\[CrossRef\]](#)
4. Gautam, A.R.; Fulwani, D.M.; Makineni, R.R.; Rathore, A.K.; Singh, D. Control strategies and power decoupling topologies to mitigate 2ω -ripple in single-phase inverters: A review and open challenges. *IEEE Access* **2020**, *8*, 147533–147559. [\[CrossRef\]](#)
5. Jang, J.; Pidaparthi, S.; Choi, B. Current mode control for LLC series resonant DC-to-DC converters. *Energies* **2015**, *8*, 6098–6113. [\[CrossRef\]](#)
6. Pan, C.T.; Lai, C.M.; Cheng, M.C. A novel high step-up ratio inverter for distributed energy resources (DERs). In Proceedings of the 2010 International Power Electronics Conference, Sapporo, Japan, 21–24 June 2010; pp. 1433–1437.
7. Liao, Y.H.; Lai, C.M. Newly-constructed simplified single-phase multistring multilevel inverter topology for distributed energy resources. *IEEE Trans. Power Electron.* **2011**, *26*, 2386–2392. [\[CrossRef\]](#)
8. Pan, C.T.; Cheng, M.C.; Lai, C.M. A novel integrated DC/AC converter with high voltage gain capability for distributed energy resource systems. *IEEE Trans. Power Electron.* **2012**, *27*, 2385–2395. [\[CrossRef\]](#)
9. Lai, C.M.; Yu, H.P.; Liu, W.C. A single-stage grid-connected microinverter with unity-power-factor for photovoltaic applications. *J. Technol.* **2015**, *30*, 25–31.
10. Fontes, G.; Turpin, C.; Astier, S.; Meynard, T.A. Interactions between fuel cells and power converters: Influence of current harmonics on a fuel cell stack. *IEEE Trans. Power Electron.* **2007**, *22*, 670–678. [\[CrossRef\]](#)
11. Ahmad, A.A.; Abrishamifar, A.; Samadi, S. Low-frequency current ripple reduction in front-end boost converter with single-phase inverter load. *IET Power Electron.* **2012**, *5*, 1676–1683. [\[CrossRef\]](#)
12. Wang, J.; Ji, B.; Lu, X.; Deng, X.; Zhang, F.; Gong, C. Steady-state and dynamic input current low-frequency ripple evaluation and reduction in two-stage single-phase inverters with back current gain model. *IEEE Trans. Power Electron.* **2014**, *29*, 4247–4260. [\[CrossRef\]](#)
13. Shi, Y.; Liu, B.; Duan, S. Low-frequency input current ripple reduction based on load current feedforward in a two-stage single-phase inverter. *IEEE Trans. Power Electron.* **2016**, *31*, 7972–7985. [\[CrossRef\]](#)
14. Zhu, G.R.; Wang, H.; Liang, B.; Tan, S.C.; Jiang, J. Enhanced single-phase full-bridge inverter with minimal low-frequency current ripple. *IEEE Trans. Ind. Electron.* **2016**, *63*, 937–943. [\[CrossRef\]](#)
15. Iyer, V.M.; John, V. Low-frequency dc bus ripple cancellation in single phase pulse-width modulation inverters. *IET Power Electron.* **2015**, *8*, 497–506. [\[CrossRef\]](#)
16. Lai, C.M. Single-stage grid-connected PV micro-inverter based on interleaved flyback converter topology. In Proceedings of the 2014 IEEE International Symposium on Computer, Consumer and Control, Taichung, Taiwan, 10–12 June 2014; pp. 187–190.
17. Chen, Y.M.; Liu, Y.C.; Wu, F.Y. Multi-input converter with power factor correction, maximum power point tracking, and ripple-free input currents. *IEEE Trans. Power Electron.* **2004**, *19*, 631–639. [\[CrossRef\]](#)
18. Wai, R.J.; Lin, C.Y. Active low-frequency ripple control for clean-energy power conditioning mechanism. *IEEE Trans. Ind. Electron.* **2010**, *57*, 3780–3792. [\[CrossRef\]](#)
19. Wai, R.J.; Lin, C.Y. Dual active low-frequency ripple control for clean-energy power-conditioning mechanism. *IEEE Trans. Ind. Electron.* **2011**, *58*, 5172–5185.
20. Liu, X.; Li, H. An electrolytic-capacitor-free single-phase high-power fuel cell converter with direct double-frequency ripple current control. *IEEE Trans. Ind. Appl.* **2015**, *51*, 297–308. [\[CrossRef\]](#)
21. Zhong, Q.C.; Ming, W.L.; Cao, X.; Krstic, M. Control of ripple eliminators to improve the power quality of DC systems and reduce the usage of electrolytic capacitors. *IEEE Access* **2016**, *4*, 2177–2187. [\[CrossRef\]](#)
22. Shimizu, T.; Suzuki, S. A single-phase grid-connected inverter with power decoupling. In Proceedings of the 2010 IEEE Power Electronics Conference, Orlando, FL, USA, 17–21 June 2007; pp. 2918–2923.

23. Liao, C.Y.; Chen, Y.M.; Lin, W.H. Forward-type micro-inverter with power decoupling. In Proceedings of the 2013 IEEE Applied Power Electronics Conference and Exposition, Long Beach, CA, USA, 17–21 March 2013; pp. 2852–2857.
24. Chen, Y.M.; Liao, C.Y. Three-port flyback-type single-phase micro-inverter with active power decoupling circuit. In Proceedings of the 2011 IEEE International Conference on Energy Conversion Congress and Exposition, Phoenix, AZ, USA, 17–22 September 2011; pp. 501–506.
25. Christidis, G.C.; Kyritsis, A.C.; Papanikolaou, N.P.; Tatakis, E.C. Investigation of parallel active filters' limitations for power decoupling on single-stage/single-phase microinverters. *IEEE J. Emerg. Sel. Top. Power Electron.* **2016**, *4*, 1096–1106. [[CrossRef](#)]
26. Lai, C.M.; Teh, J.; Cheng, Y.H. An efficient active ripple filter for use in single-phase DC-AC conversion system. In Proceedings of the 2017 IEEE 8th International Conference on Awareness Science and Technology, Taichung, Taiwan, 8–10 November 2017; pp. 234–237.
27. Lai, J.S.; Ellis, M.W. Fuel cell power systems and applications. *Proc. IEEE* **2017**, *105*, 2166–2190. [[CrossRef](#)]
28. Kim, N.; Parkhideh, B. Power pulsation decoupling in a series-stacked PV- battery inverter. In Proceedings of the 2019 IEEE Applied Power Electronics Conference and Exposition, Anaheim, CA, USA, 17–21 March 2019.
29. Takaoka, N.; Watanabe, H.; Itoh, J.I. Isolated DC to single-phase AC converter with active power decoupling capability for battery storage system. In Proceedings of the 2019 8th International Conference on Renewable Energy Research and Applications, Brasov, Romania, 3–6 November 2019; pp. 739–743.
30. Jiang, J.; Pan, S.; Zha, X.; Hao, L. A new single-phase single-stage photovoltaic grid-tied inverter with leakage current eliminating and power decoupling. In Proceedings of the 2019 8th IEEE International Symposium on Power Electronics for Distributed Generation Systems, Brasov, Romania, 3–6 November 2019; pp. 560–564.
31. Lai, C.M.; Lin, Y.J.; Cheng, Y.H.; Yao, L. Development of a modular single-phase grid-tie inverter system for fuel-cell power generation. *J. Chin. Inst. Eng.* **2018**, *41*, 112–123. [[CrossRef](#)]
32. Lai, C.M.; Lin, Y.C. Active Power Compensation Circuit. Taiwan Patent No. I559659, 21 November 2016.
33. Lai, C.M.; Lin, Y.C. Active Power Compensation System. Taiwan Patent No. I590554, 1 July 2017.



© 2020 by the authors. Licensee MDPI, Basel, Switzerland. This article is an open access article distributed under the terms and conditions of the Creative Commons Attribution (CC BY) license (<http://creativecommons.org/licenses/by/4.0/>).

© 2020. This work is licensed under
<http://creativecommons.org/licenses/by/3.0/> (the “License”). Notwithstanding
the ProQuest Terms and Conditions, you may use this content in accordance
with the terms of the License.